



Exploring a geophysical process-based attribution technique for the determination of the atmospheric boundary layer depth using aerosol lidar and near-surface meteorological measurements

Sandip Pal, M. Haeffelin, E. Batchvarova

► To cite this version:

Sandip Pal, M. Haeffelin, E. Batchvarova. Exploring a geophysical process-based attribution technique for the determination of the atmospheric boundary layer depth using aerosol lidar and near-surface meteorological measurements. *Journal of Geophysical Research: Atmospheres*, 2013, 118 (16), pp.9277-9295. 10.1002/jgrd.50710 . hal-01092232

HAL Id: hal-01092232

<https://hal.science/hal-01092232>

Submitted on 22 Oct 2021

HAL is a multi-disciplinary open access archive for the deposit and dissemination of scientific research documents, whether they are published or not. The documents may come from teaching and research institutions in France or abroad, or from public or private research centers.

L'archive ouverte pluridisciplinaire **HAL**, est destinée au dépôt et à la diffusion de documents scientifiques de niveau recherche, publiés ou non, émanant des établissements d'enseignement et de recherche français ou étrangers, des laboratoires publics ou privés.

Copyright

Exploring a geophysical process-based attribution technique for the determination of the atmospheric boundary layer depth using aerosol lidar and near-surface meteorological measurements

Sandip Pal,^{1,2} Martial Haeffelin,³ and Ekaterina Batchvarova⁴

Received 24 January 2013; revised 25 July 2013; accepted 2 August 2013; published 30 August 2013.

[1] A new objective method for the determination of the atmospheric boundary layer (ABL) depth using routine vertically pointing aerosol lidar measurements is presented. A geophysical process-based analysis is introduced to improve the attribution of the lidar-derived aerosol gradients, which is so far the most challenging part in any gradient-based technique. Using micrometeorological measurements of Obukhov length scale, both early morning and evening transition periods are determined which help separate the turbulence regimes during well-mixed convective ABL and nocturnal/stable ABL. The lidar-derived aerosol backscatter signal intensity is used to determine the hourly-averaged vertical profiles of variance of the fluctuations of particle backscatter signal providing the location of maximum turbulent mixing within the ABL; thus, obtained mean ABL depth guides the attribution by searching for the appropriate minimum of the gradients. An empirical classification of the ABL stratification patterns into three different types is proposed by determining the changes in the near-surface stability scenarios. First results using the lidar observations obtained between March and July in 2011 at SIRTa atmospheric observatory near Palaiseau (Paris suburb) in France demonstrate that the new attribution technique makes the lidar estimations of ABL depth more physically reliable under a wide spectrum of meteorological conditions. While comparing lidar and nearby radiosonde measurements of ABL depths, an excellent concordance was found with a correlation coefficient of 0.968 and 0.927 for daytime and nighttime measurements, respectively. A brief climatology of the characteristics of the ABL depth, its diurnal cycle, a detailed discussion of the morning and evening transitions are presented.

Citation: Pal, S., M. Haeffelin, and E. Batchvarova (2013), Exploring a geophysical process-based attribution technique for the determination of the atmospheric boundary layer depth using aerosol lidar and near-surface meteorological measurements, *J. Geophys. Res. Atmos.*, 118, 9277–9295, doi:10.1002/jgrd.50710.

1. Introduction

[2] The atmospheric boundary layer (ABL) and the entrainment zone at the top of the ABL primarily govern the mixing of aerosol particles and other gaseous species (e.g., CO₂, CO, CH₄, etc.) in the lower troposphere, with consequences for air quality and climate simulation [Stull, 1988]. Since the depth of the ABL acts as a “first-order” control or a mixing volume for aerosol and climate-forcing constituents, it is considered to be an important parameter for

characterizing atmospheric processes like dispersion and transport of aerosol particles in realistically variable boundary layer structures [e.g., Maronga and Raasch, 2012], aerosol formation [e.g., Nilsson *et al.*, 2001], near-surface aerosol concentration [e.g., Pal and Devara, 2012], and often used as a scaling parameter for the ABL parameterizations [Moeng, 1984].

[3] The investigation of the ABL depth variability is also important for meteorological process studies like convection initiation including cloud formation and transitions within the boundary layer [e.g., Behrendt *et al.*, 2011a; Hogan *et al.*, 2009], vertical transport of heat and moisture [e.g., Couvreux *et al.*, 2007], and interactions between the boundary layer and the free atmosphere (FA) [e.g., Lenschow *et al.*, 2012]. Additionally, since the ABL depth is a key scaling parameter for monitoring of pollution and budget analyses of greenhouse gases, recently, a large number of networks and programs have been initiated like ICOS (Integrated carbon observing system) [Ramonet *et al.*, 2011], EG-CLIMET COST action [Haefelin *et al.*, 2012], etc. Hence, there is a strong need of a robust technique for routine monitoring of the ABL depth.

¹Laboratoire de Météorologie Dynamique, CNRS-Ecole Polytechnique, Palaiseau, France.

²Department of Environmental Sciences, University of Virginia, Charlottesville, Virginia, USA.

³Institut Pierre-Simon Laplace, CNRS-Ecole Polytechnique, Paris, France.

⁴National Institute of Meteorology and Hydrology, Bulgarian Academy of Sciences, Sofia, Bulgaria.

Corresponding author: S. Pal, Laboratoire de Météorologie Dynamique, CNRS-Ecole Polytechnique, FR-91128 Palaiseau CEDEX, France. (sandip.pal@lmd.polytechnique.fr, sp5hd@virginia.edu)

[4] The ABL depths can be determined from the radio-sonde-derived profiles of thermodynamic variables like temperature, humidity, and horizontal wind speed, however, only infrequently [Seibert *et al.*, 2000]. The difficulty in directly observing the thermodynamic structures of the atmosphere makes ground-based remote sensing technique an attractive choice [e.g., Pal *et al.*, 2008]. For instance, elastic-backscatter lidar and ceilometer provide vertical profiles of backscatter from aerosol particles and molecules in the atmosphere [e.g., Eresmaa *et al.*, 2006, 2012; Emeis *et al.*, 2007; Mönkel, 2007; Behrendt *et al.*, 2011b]. Because of the effect the ABL has on aerosol stratification, it is possible to use aerosol backscatter as a proxy for the ABL inversion [e.g., Stull, 1988; Wulfmeyer *et al.*, 2010].

[5] Different algorithms are used to determine the ABL depths from lidar and ceilometer measurements [e.g., Haeffelin *et al.*, 2012]. A particular limitation of the existing gradient-based algorithms is that since aerosol may lay in multiple stratifications, often several local minima do occur in the profile of gradient of aerosol backscatter. Hence, the choice of the relevant (“true”) minimum is generally not well specified [e.g., Menut *et al.*, 1999; Pal *et al.*, 2010]. For the determination of the stable boundary layer (SBL) depths and/or the growing convective boundary layer (CBL) depths in the morning, many researchers use the Haar wavelet technique where they subjectively constrain the upper limit to the base of the residual layer (RL) [e.g., Gan *et al.*, 2011]. To summarize, considerable progress has been made to date on the application of gradient-based algorithms to identify distinct atmospheric layers using lidar measurements. However, the major challenge that still lies in most of the today’s ABL height detection methods is the application of an automated and robust attribution technique, in particular, for operational lidar monitoring of the ABL. Additional demands include high temporal resolution and retrieval of uncertainties in the ABL depth time series.

[6] Very recently, Haman *et al.* [2012] found that during the early evening transition (EET) period when convection is weakening and a new nocturnal boundary layer (NBL) is forming, high uncertainty and inaccuracy result for the NBL depths. In particular, Haeffelin *et al.* [2012] illustrated that during the EET, the strongest aerosol gradient corresponds mainly to the RL, until new aerosols, generated at the ground, become sufficiently concentrated to provide a renewed strong gradient able to produce a detectable low-level inflection point. On the other hand, Granados-Muñoz *et al.* [2012] illustrated that during the early morning transition (EMT) period when RL frequently appears in the lower most troposphere, lofted aerosol layers do not represent the growing CBL depths and finally emphasized the requirement of additional information or measurements to correctly determine the ABL depths. De Giuseppe *et al.* [2012] introduced supplementary information consisting of a Bayesian selective method, a boundary layer model simulation, and the ABL depths climatology for the purpose of attribution. However, no attention was paid to the boundary layer processes during the EMT and the EET periods for the purpose of attribution. The EMT period refers to the period from sunrise to the time when the SBL is eroded and rapid growth in the CBL depth is observed; during this time the ABL changes from a stable to an unstable regime. The EET period refers

to the period from sunset to the time when an NBL is formed near the surface.

2. Site, Instrumentation, and the Data Sets

[7] We used a vertically pointing aerosol lidar transmitting laser radiation at 355 nm wavelength with a pulse energy of 16 mJ at 20 Hz repetition rate (ALS-450, commercialized by Leosphere) for the measurements of the ABL aerosol stratification. The aerosol backscatter measurements with the ALS-450 with an operational range of 150 – 12,000 m are routinely performed at the SIRTa (Site Instrumental de Recherche par Télédétection Atmosphérique) observatory near Palaiseau (48.7°N, 2.21°E, and 156 m ASL), France. SIRTa is located on a 10 km wide plateau at approximately 20 km south of Paris. Further information on the different instruments at SIRTa including the ALS-450 and a detailed description of the site can be found elsewhere [Haeffelin *et al.*, 2005].

[8] Campbell Scientific’s CSAT3 3-D sonic anemometer is installed at 10 m above ground level (AGL) on a mast that is routinely operated at SIRTa. These measurements are used to calculate the momentum and sensible heat flux and to determine the Obukhov length scale, L [Obukhov, 1971]. We use the 10 min averaged values of the three components of wind (u , v , w) and sonic temperature (T) to calculate fluctuations of these parameters. Measurements of temperature, pressure, humidity, and precipitation obtained at 2 m as well as 30 m are also used. Sunrise and sunset for SIRTa are determined from astronomical calculations, with times in UTC. Routine radiosonde (RS) launches are performed twice a day at the French national weather service station at Trappes (48.78°N, 2.00°E, 167 m ASL), located 12 km west of SIRTa. The RS-based thermodynamic profiles are used to determine the ABL depths to evaluate lidar-based results.

3. Basic Concept of the Paper

[9] For a comprehensive discussion on the research concept applied, a simple scheme showing the entire diurnal cycle of the ABL depth evolution over land is presented in Figure 1. In an SBL, aerosols are, in general, stratified in many different layers where turbulence features are often weak and of discontinuous character [Stull, 1988]. Hence, if only gradient-based techniques are applied on the lidar aerosol backscatter profiles, the strongest gradients will often occur at the top of the RL and at heights of other aerosol layers (e.g., as a result of advection) but not necessarily at the SBL top [e.g., Gan *et al.*, 2011]. Within the daytime quasi-stationary CBL, aerosol particles are, in general, well mixed, and a strong inversion is often present at the interface between aerosol-laden CBL and relatively cleaner FA (Figure 1). In such situations, gradient techniques often fail to discriminate the top and bottom of the entrainment zone [e.g., Mattis *et al.*, 2004; Pal *et al.*, 2010]. Stull [1988] illustrated that during the EET after the collapse of the turbulence near the ground, although decaying turbulence exists in the RL for some time, the NBL starts to develop while the daytime well-mixed CBL top remains at about the same height and survives as a RL.

[10] Within this work, we seek a technique to objectively determine the ABL depth that could be based on the measurements from surface meteorological instruments and the most

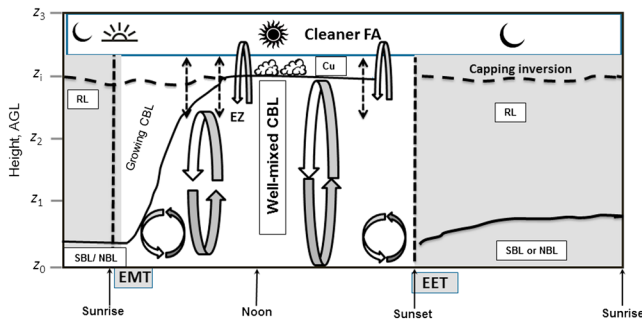


Figure 1. A simplified scheme displaying the life cycle of the clear-sky continental atmospheric boundary layer (ABL) (adapted from *Stull*, 1988). Shaded field marks night; white represents day. Solid line marks top of the ABL while the dashed line shows the level of the RL, z_1 , z_2 , etc. indicate heights above ground level (AGL), and z_1 marks the top of the ABL. Black solid arrows at bottom mark sunrise, noon, and sunset. Curved arrows show the convectively driven turbulent eddies and plumes. Entrainment process near the top of the ABL is marked by dashed arrows. CBL: convective boundary layer, Cu: Cumulus clouds, EMT: early morning transition, EET: early evening transition, EZ: entrainment zone, FA: free atmosphere, NBL: nocturnal boundary layer, SBL: stable boundary layer.

commonly used lidar system, i.e., a ground-based vertically pointing aerosol lidar with a key emphasis on a robust attribution technique. A flowchart including the key components of the method introduced is displayed in Figure 2. The lidar-based ABL depth determination is essentially a two-step procedure: detection of gradients and attribution. Locations of major aerosol gradients are obtained by applying the STRAT-2D (structure of the atmosphere) algorithm

[*Morille et al.*, 2007; *Haefelin et al.*, 2012] on the profiles of range-square corrected lidar signal intensity; the attribution step involves assigning the height of one of the detected layers to the instantaneous ABL top height which is mainly guided by variance-based technique via determination of mean ABL depth (see sections 4.6 and 5.1).

[11] On the other hand, the near-surface micrometeorological measurements are used to determine the stability regimes of the surface using the Obukhov length scale. Near-surface meteorological characteristics during the EMT govern the boundary layer processes including the strength and size of the turbulent eddy, erosion of the SBL, and finally the growth of the CBL throughout the morning [*Batchvarova and Gryning*, 1991, 1994]. The time series of potential temperature is used to estimate a first-order approximation of the ABL depth growth rate. Then, the end times of both the EMT and the EET periods are robustly determined either using changes in the stability regimes or the growth rates of ABL depth or combination of both. The EMT and the EET are determined to assist the attribution via separating the two regimes of the ABL, namely, the CBL and the SBL. The CBL regime is considered for the period between the end of the EMT and the end of the EET while the SBL regime corresponds to the period between the end of EET and the next day EMT.

[12] Using some predefined criteria, variance-derived mean ABL depths for both the CBL and the SBL regimes are then obtained which unambiguously facilitates the attribution of the instantaneous “true” ABL depth by selecting one of the STRAT-2D derived heights. Prior to that, the STRAT-2D layers are processed using additional criteria based on the growth rates obtained from the encroachment model, variability in the Cu clouds (if present), etc. Finally, a high-resolution (i.e., temporal resolution of 10 min) time series of the instantaneous ABL depths for the entire diurnal

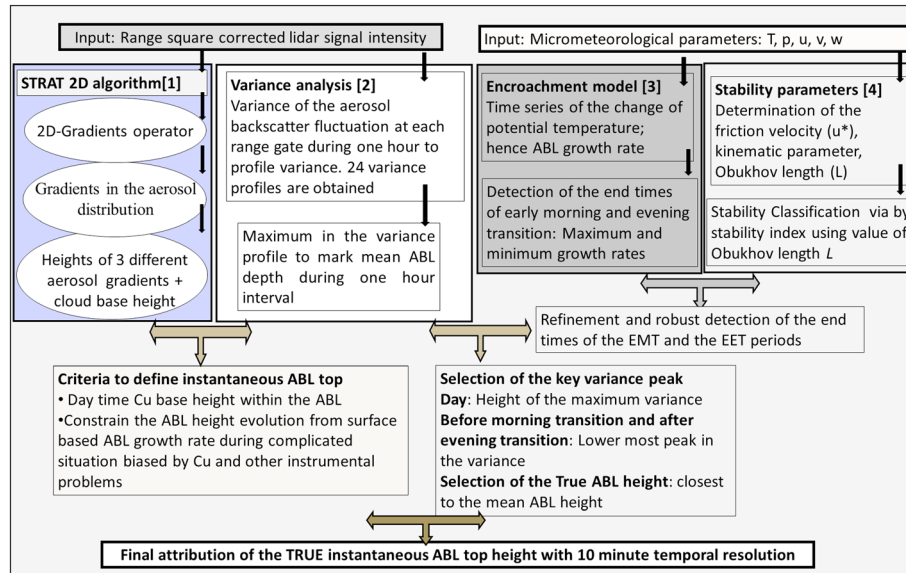


Figure 2. Flow chart for the data analysis methodology to derive high-resolution instantaneous ABL depth from lidar measurements which involves three major components: determination of three key heights of aerosol stratifications and cloud base heights by STRAT-2D, variance-based method for profiling turbulence features, and estimation of ABL growth rates and L from near-surface micrometeorological measurements.

Table 1. Determination of Stability Regimes and Corresponding Indices Using the Obukhov Length L

Ranges of the Obukhov Length L (m)	Stability Regime	Stability Index
$10 < L < 200$	Stable	1
$200 < L < 500$	Near neutral	2
$L > 500$ or $L < -500$	Neutral	3
$-500 < L < -200$	Near neutral unstable	4
$-200 < L < -100$	Unstable	5
$-100 < L < -10$	Very unstable	6

cycle is obtained. In the following two sections, we discuss different components of the methodology in detail.

4. Major Steps for the Objective Attribution

4.1. Determination of Temporal Variation of Atmospheric Stability

[13] The detection of the stability regimes near the surface is performed by determining the Obukhov length scale (L), which is the ratio of the surface fluxes of momentum and buoyancy. The sensible heat flux Q_H is determined following the eddy covariance technique [Stull, 1988] as

$$Q_H = c_p \rho \overline{w'T'} \quad (1)$$

where Q_H is positive in the upward direction, w is the vertical velocity, T is the sonic temperature, the prime indicates a fluctuation from a mean (over 10 min), ρ is the air density, and c_p is the specific heat of air at constant pressure. The turbulence term $\overline{w'T'}$ in equation (1) is called the “kinematic” parameter and is used to determine the crossover times in the morning and the evening (see sections 4.3 and 4.4). The crossover is defined as the time when kinematic parameter changes sign: negative to positive during the EMT and vice versa during the EET. L is determined following

$$L = -u_*^3 T \rho c_p / 0.4 g Q_H \quad (2)$$

where g is the gravitational acceleration and u_* is the friction velocity determined by three components (u , v , and w) of the wind vector as

$$u_*^2 = \sqrt{(\overline{u'w'})^2 + (\overline{v'w'})^2} \quad (3)$$

[14] Finally, the stability classification is performed using L [Gryning *et al.*, 2007]. Additionally, to obtain a clear picture of the diurnal cycle of the stability regimes, an index is introduced that helps investigate the stability regimes from the nighttime SBL through growing CBL in the morning to the daytime well-mixed CBL. For brevity, we call it a stability index that varies from 1 to 6. Table 1 illustrates the different stability indices used in this study.

4.2. First-Order Approximation of the ABL Depth Growth Rate

[15] A first-order approximation of the growth rate of the ABL depths can be obtained following an encroachment model [e.g., Stull, 1988]. The encroachment model used focuses only on the thermodynamics (the heating from the surface only and neglecting heating from entrainment). It is also assumed that the vertical gradient of the potential temperature (θ), $d\theta/dz$, is

zero in the CBL. Under this assumption, the relationship between θ and ABL depth h , is given by [Stull, 1988]

$$\frac{d\theta}{dt} = \gamma \frac{dh}{dt} \quad (4)$$

where t denotes time and γ is lapse rate which could be estimated from the radiosonde observation and is assumed to be constant during a day. Finally, the maximum ABL growth rate is estimated and used in the analyses which help detect the both transition times of a day.

4.3. Early Morning Transition

[16] The EMT period between NBL and daytime well-mixed CBL regimes can be investigated using the temporal evolution of the near-surface state variables [e.g., Kaimal *et al.*, 1976]. Tennekes [1973] defined the morning transition as the “initial filling of the nocturnal inversion.” After sunrise, the near-surface air temperature rises, but, as will be shown, the turbulent heat flux does not become positive until later.

[17] The EMT period is referred to as the period starting from sunrise through the crossover of Q_H to the time when stability index changes from 1 to 5 or 6. We used the kinematic parameter of Q_H (equation (2)) to determine the time of crossover, i.e., when it becomes positive. Consequently, after the crossover and at the end of the EMT period, the stability near the surface decreases and the depth of the ABL starts growing. Thus, when L -based stability index (henceforth, stability index) reaches a value of 5 or 6, we define the corresponding time to be the end of the EMT period. After the EMT, Q_H , in general, starts to increase linearly in time as does the near-surface temperature. We found that on many days, the stability index makes a direct transition from a stable to an unstable or a very unstable regime; however, similar direct transitions do not occur on all days but indirectly through stability classes 3 and 4 which mainly depend upon the strength of the inversions in the SBL.

[18] Additionally, the first-order approximation of ABL depth growth rates (equation (4)) is further investigated and we find that the time of the maximum heating coincides with the end of the EMT period. However, it should be noted with sufficient care that the encroachment model provides only a “first-order approximation” on the ABL depth growth rates by mainly considering convective turbulence (buoyant production) [Kaimal and Finnigan, 1994]. Therefore, the criterion based on the ABL growth rates for determining the end of the EMT period is only used during the situations when the stability index did not show any kind of transitions from stable or neutral regimes to unstable or very unstable regimes.

4.4. Early Evening Transition

[19] An objective determination of the EET period is also performed so that the key physical processes (e.g., decrease of vigorous turbulence) can be detected and a definition for the end of the EET when the NBL starts developing can be obtained. Following Caughey *et al.* [1979], we used the widely accepted definition of the crossover during the EET which indicates the time when the near-surface heat flux changes sign (positive to negative). We used only the kinematic term of the sensible heat flux (see equation (4)) to detect the time of crossover.

[20] Acevedo and Fitzjarrald [2001] illustrated a decrease in the CBL turbulence activity after sunset during the EET. A decrease in the stability index implies a decrease in the

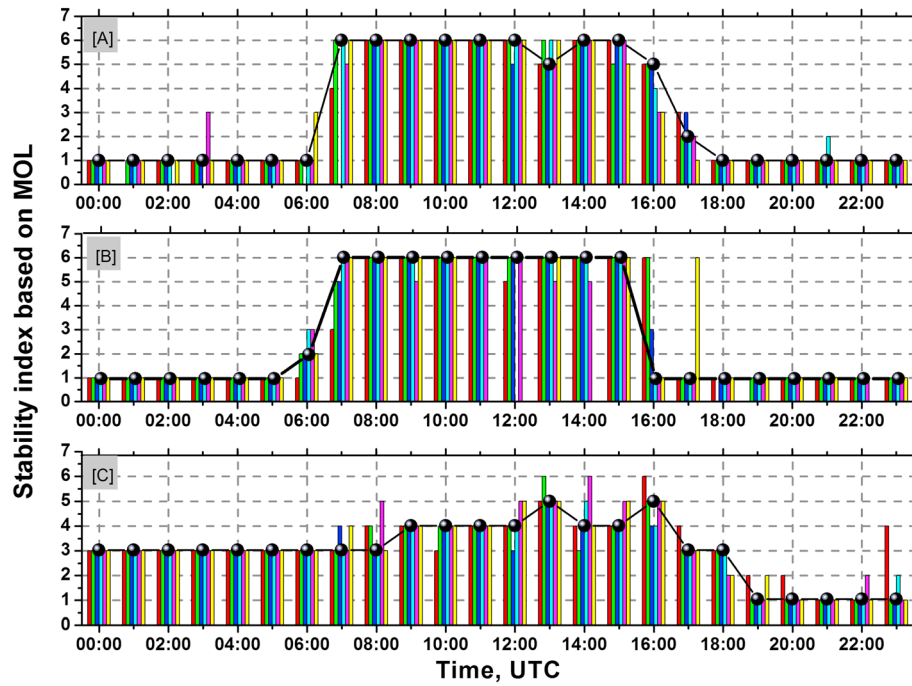


Figure 3. (a): Frequency distribution of six different stability classes over 1 h during the entire diurnal cycle for the determination of the end of the EMT and the EET for type Ia transition. Colored vertical columns mark six 10 min averaged values of the stability index during an hour. The proper determination of stability index during an hour is performed by finding the most frequent value among them. A solid line with sphere overlaid indicates the finally attributed stability index. (b) and (c): same as Figure 3a but for types IIa and IIIa, respectively.

turbulence intensity when ABL turbulence cannot maintain its vigorous mixing characteristics; hence, mixing of the larger eddies and consequent stronger turbulence features cease. Thus, the stability index could be used for an indicator for the time when the NBL starts to evolve. We found that stability index changes from 5 or 6 to 1 at the end of EET period. We define the end of EET time when the stability index reaches 1 (stable regime, see Table 1). Additionally, we found that the time of the maximum decay (or maximum cooling) in the ABL depths following the encroachment model coincides with the end of the EET time. We used the latter definition of the end of EET time only for the situations when a change in the stability index from 5 or 6 to 1 was not detected.

[21] Cumulative percentages of 10 min temporally resolved L for an interval of an hour are first obtained. The proper determination of stability during an hour is performed using the most frequent value out of six 10 min averaged values. Figure 3 shows the frequency distribution of the six different stability classes during 1 h averaging period for three different classes, namely, types I, II, and III observed on three different days at SIRTa; see section 5.2 for an empirical classification of ABL depth evolution. For instance, Figure 3 illustrates a direct transition (type I) to robustly detect the end of the EMT when the stability index changes from 1 to 6. The end of the EET is determined when the stability index reaches 1.

4.5. 2D-Gradient Method to Determine Instantaneous ABL Depth

[22] The STRAT algorithm analyzes the range-squared corrected backscatter signal to retrieve mixing heights based

on a first derivative of the Gaussian wavelet covariance analysis. This algorithm mainly consists of four successive steps performed on each lidar profile: noise detection via determination of signal-to-noise ratio at each height step, molecular layer detection, particle layer detection with separate cloud, and aerosol layer identification [Morille *et al.*, 2007]. Haefelin *et al.* [2012] used an improved ABL depth detection method STRAT-2D where they introduced a new edge detection method based on both vertical and temporal gradients in the attenuated backscatter. Thus, using STRAT-2D, locations of three key aerosol gradients (two strongest gradients and the lowest gradient) within and above the ABL and the cloud base heights with a temporal resolution of 10 min are identified which are then used for the attribution step to finally determine the time series of instantaneous ABL depths. Further detailed description of the STRAT-2D can be found in Haefelin *et al.* [2012].

4.6. Variance Method to Determine Mean ABL Depth

[23] Using variance-based technique, many researchers estimated mean ABL depth from lidar backscatter measurements [e.g., Lammert and Bösenberg, 2006; Pal *et al.*, 2010]. Profiles of the variance of fluctuations of particle backscatter $\beta'_{\text{par}}(t, z)$ are derived using the approach outlined by Lenschow *et al.* [2000]. The raw aerosol backscatter data were analyzed from 150 to 3500 m with high spatial (10 m) and temporal (30 s) resolution. An overall averaging time is typically 1 h for each variance profile.

[24] The time series of $\beta'_{\text{par}}(t, z)$ at different heights are high-pass filtered at a cutoff time period of 30 min to minimize the influence of mesoscale variability. High-pass

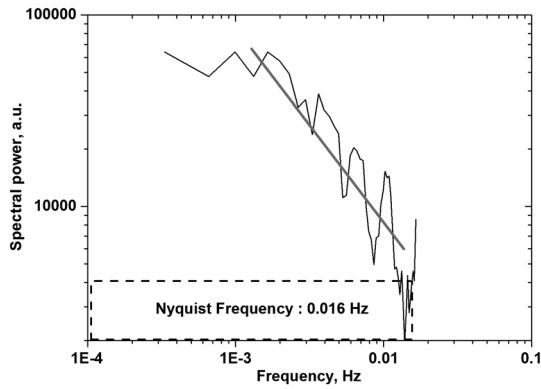


Figure 4. An FFT-based spectral analysis to estimate both atmospheric and noise variance from lidar measurements at a height of 855 m AGL. On the log-log spectra, a solid sloped line indicates the $-5/3$ power law curve confirming the inertial subrange. A rectangular box marks the region of the spectrum to estimate the noise variance calculated from the high tail of the frequency spectrum (0.8 to 1.0 of the Nyquist frequency).

filtering is performed in a frequency space by multiplying the Fourier transform with a filter function. We consider a cosine function as an appropriate filter function following Wulfmeyer *et al.* [2010]. An FFT power spectrum of the detrended and high-pass filtered time series of $\beta'_{\text{par}}(t, z)$ is then obtained up to Nyquist frequency. Figure 4 displays an example of a variance spectrum of $\beta'_{\text{par}}(t, z)$ for a height of 855 m AGL during a period when the CBL is well mixed.

Spectral variance determined follow Kolmogorov's $-5/3$ power law which confirms that an inertial subrange is present at this level as this lies within the CBL. The power spectrum also confirms the presence of the dissipation range near the high-frequency tail where the classical power law scaling does not exist. Total variance is calculated from the area covered by the spectra in the frequency versus amplitude space. Then, in a similar fashion, the noise variance is calculated from the high tail of the frequency spectrum (0.8 to 1.0 of the Nyquist frequency). Finally, atmospheric variance is calculated by subtracting the noise variance from total variance. Similar analysis is performed at each height step to obtain a variance profile. The mean ABL depth (over an hour) is determined from the maximum in the variance profile which helps attribute the instantaneous ABL depth as described in section 5.

[25] Figure 5 shows three characteristic variance profiles determined for three different time periods on 24 March 2011 which confirms the location of maximum variability at the top of the CBL or the NBL. Given the scope of the paper, we are mainly interested in the characteristic of the vertical distribution of the variance and the location of its maximum for the determination of the mean ABL depths.

5. Final Attribution for Determining ABL Depth

5.1. Combined Approach

[26] The daily lidar data set is split into 23 intervals of appropriate length—here, 1 h—which is analyzed to obtain the variance profile. For the CBL regime, the maximum in

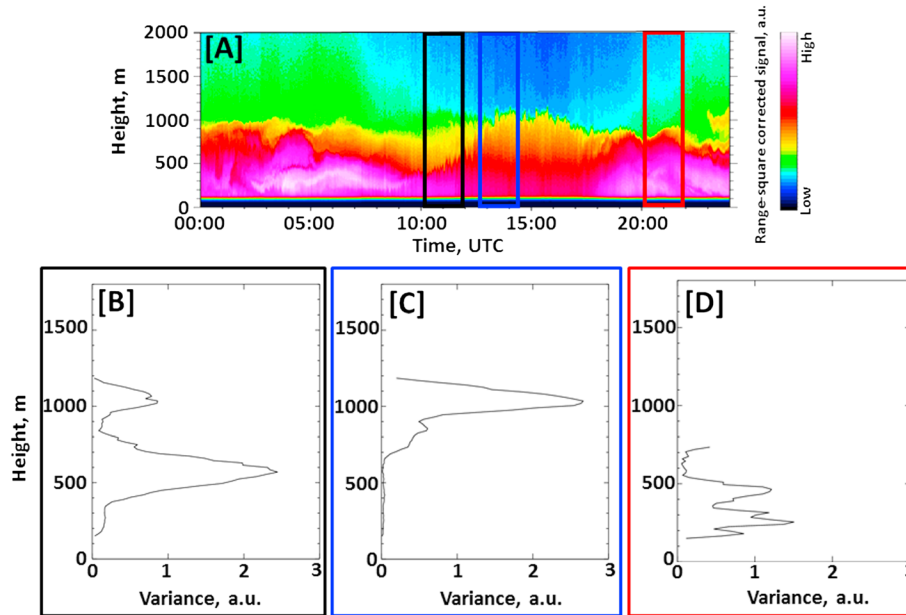


Figure 5. An example illustrating the retrieval of mean ABL depth by the variance analysis using the lidar measurements obtained on 24 March 2011 over SIRTA observatory. (a): Time-height cross section of the range-squared corrected lidar signal intensity during the entire diurnal cycle. Vertically aligned color bar (in linear scale) on the right indicates the intensity in arbitrary units. Sunrise and sunset times on this day are 05:55 and 18:15 UTC, respectively. Variance profile obtained during (b): the developing CBL regime with RL atop in the morning, (c): the well-mixed CBL in the afternoon, and (d): the SBL regime prevailing during the evening. Colored boxes mark the different time intervals considered for the variance analysis. The maximum in the variance profile corresponds to the mean ABL depth for 1 h interval considered. The heights in all panels are in m AGL.

Table 2. Different Classes of the Atmospheric Boundary Layer Circulation Types Considered in the Study

Classes of Boundary Layer Circulation Patterns	Transition of L -Based Stability Index	Maximum dh/dt Estimated (m/h) During Early Morning Transition	Presence of Clouds
CLASS Ia	Direct/Rapid	200	Clear sky
CLASS Ib	Direct/Rapid	200	Cloud covered or Cu at the top of the growing convective boundary layer (CBL)
CLASS IIa	Indirect/slow through neutral to unstable	200 or less	Clear sky
CLASS IIb	Indirect/slow through neutral to unstable	100 or less	Cloud covered or Cu at the top of the growing CBL
CLASS IIIa	Neutral stability at sunrise or no clear transition from stable to unstable	200 or less	Clear sky
CLASS IIIb	Neutral stability at sunrise or no clear transition from stable to unstable	100 or less	Cloud covered

the variance profiles unambiguously determine the mean ABL depth. For the NBL, variance profiles often consist of two to three peaks in height for the NBL regime. We choose the mean NBL depth to be the altitude of the lowermost peak in the variance profile. We found that for the NBL, very often, the lowermost layers derived with the STRAT-2D are attributed to be the final NBL top. Using variance analysis, we obtained a time series of the mean ABL depth with a temporal resolution of 1 h. For each 1 h interval, the STRAT-2D method is applied with a temporal resolution of 10 min within a prescribed height interval around the result of the variance analysis. The variance-based results are used for the attribution by selecting the closest STRAT-2D layer from the mean ABL depth. Thus, we could obtain the finally attributed ABL depths for the time when the variance-based ABL depths are available. For the time in between two variance profiles, we choose the ABL top out of the STRAT-2D-derived layers which is closest to the variance-estimated ABL depths following

$$z_i \approx Z + \frac{dh}{dt} \quad (5)$$

where z_i is the instantaneous ABL height to be determined or compared with the STRAT-2D output, Z is the mean ABL depth obtained from the variance analysis, and dh/dt is the growth rate of the instantaneous boundary layer height obtained by using a simple encroachment model. Equation (5) also helps restrict the erroneous values of the ABL depths during attribution. Similar variance analyses were previously performed by Lammert and Bösenberg [2006]; however, this was done only for some case studies and for daytime CBL regimes.

[27] We use additional criteria to restrict the variance analyses and hence determination of mean ABL depths. For instance, the local climatology of the ABL depths is used which constrain the “true” boundary layer top height to be below 3000 m AGL (midlatitude extreme ABL depth [Seidel *et al.*, 2010]). Their results are also consistent with other studies [e.g., Menut *et al.*, 1999; Morille *et al.*, 2007; Pal *et al.*, 2012]. The variance analysis is not performed beyond this height. The STRAT-2D derived layers lying beyond this limit are also excluded for the final attribution.

[28] The base of the boundary layer Cu appearing during the daytime is considered to be the top of the CBL. The top of the CBL is the level of inversion capping the cloud layer that supports the hypothesis [Stull, 1988]. Additionally, because of the high absorption and scattering within clouds, the lidar received backscatter signal is not reliable within and above clouds. During such situations, the variance

calculation is performed to the base of the Cu obtained by STRAT-2D. Otherwise, cloud-induced noise or detector overloading dominates in the lidar signal making the ABL depth determination erroneous.

5.2. An Empirical Classification of ABL Depth Evolution

[29] The characteristics of ABL over any site differ each day due to different forcing mechanisms like the changes in the surface solar radiation, precipitation patterns, low level mesoscale convergence, advection, synoptic scale patterns, etc. [Bianco *et al.*, 2011]. Very recently, Ouwersloot *et al.* [2012] classified radiosonde measurements of ABL depths during different days. They were able to classify only 25% profiles into boundary layer types as a result of the observed transitional characteristics of the ABL which confirms that the classification of ABL regimes is a challenging task.

[30] To facilitate the analyses of the finally attributed ABL depths, we objectively classify the boundary layer circulation patterns in three different types by using the stability index and the first-order approximation of the ABL depth growth rates. Table 2 presents an overview of the different classes considered in this study. For instance, type I corresponds to a classical ABL regime where only the surface-driven processes play a key role in the absence of clouds within the ABL so that direct transition in stability index (stable to unstable) can be observed. Type II is defined as the transition when the stability index does not change from 1 to 5 or 6 but through stability index 2 or 3 while type III includes the cases where the stability index neither show any significant transition like in type I/II nor any clear transition during the entire diurnal cycle. For type III, therefore, we define the end of EMT as the time when the maximum ABL growth rate takes place. Finally, each type is subdivided into two more categories depending on the presence of clouds as obtained from the STRAT-2D (Table 2). For instance, type Ia includes clear-sky days while type Ib marks the days with direct transition but with extensive cloud cover or with CBL clouds (Cu).

6. Results and Discussion

6.1. Measurement Examples for the Three Different Classes

[31] Some measurement examples are presented here for three different types of transitions during entirely different ABL regimes to demonstrate the potential of the newly developed technique. Figure 6a illustrates an example for type Ia transition (i.e., direct transition in the stability index for

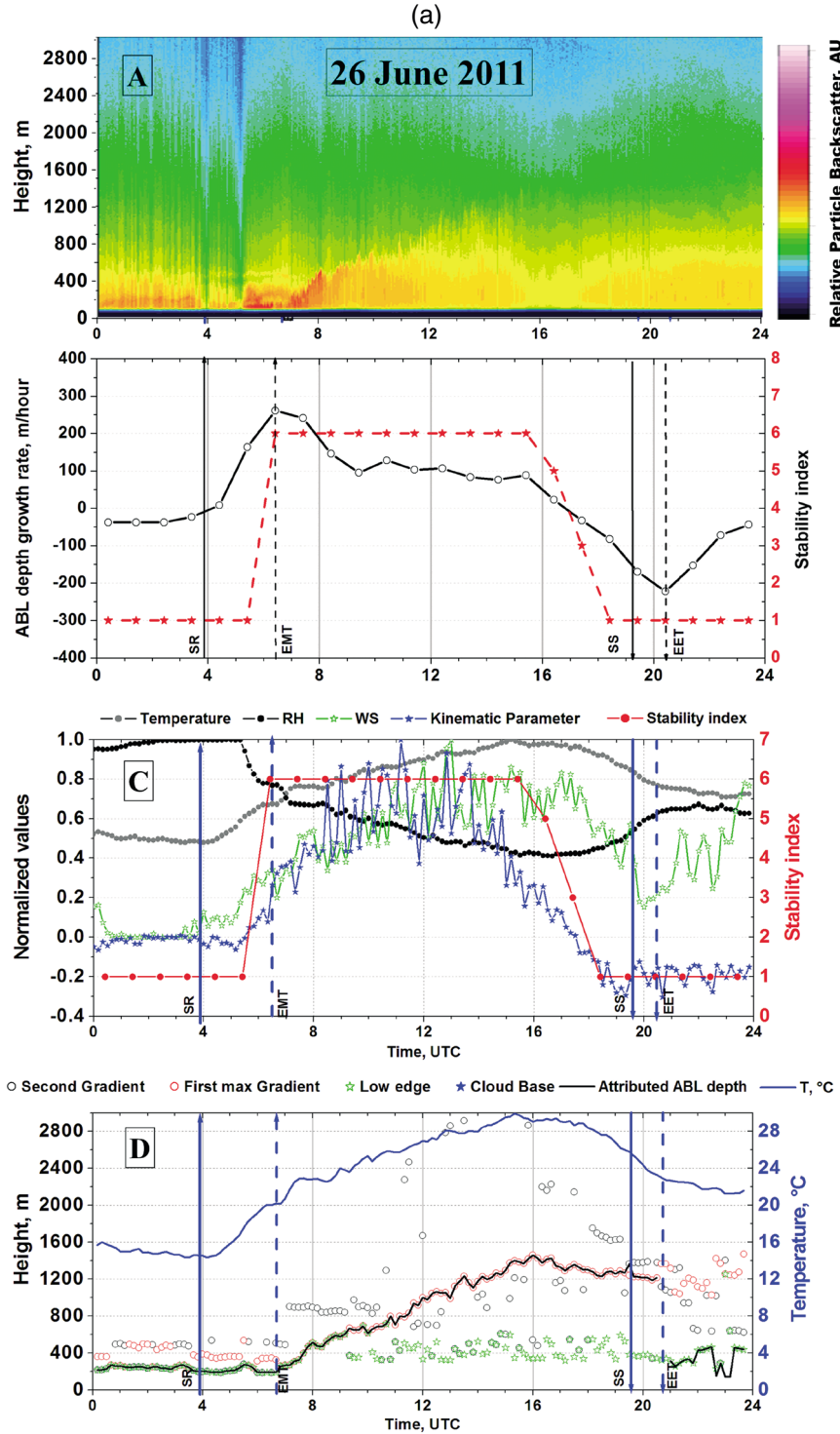


Figure 6. (a) Determination of the instantaneous ABL depths from aerosol lidar measurements over SIRTa on 26 June 2011. Heights in all panels are in m AGL. (a): Time-height cross section of range-square corrected signal intensity. Temporal and spatial resolutions in the lidar data are 30 s and 15 m, respectively. (b): Diurnal cycles of L -based stability index and ABL depth growth rates, vertical dotted lines mark the end times for the EMT and the EET periods and the solid lines mark the times of sunrise (SR) and sunset (SS), (c): Normalized values of near-surface temperature, relative humidity, wind speed, kinematic parameter. Stability index values are also overlaid (in red). RH: relative humidity, WS: wind speed, (d): STRAT-2D derived aerosol layers and cloud base heights (colored symbols) along with the finally attributed ABL depths (solid black line) and temperature (solid blue line, see right y axis for the temperature scale). Temporal resolutions in the STRAT-2D layers, finally attributed ABL depths, and 2 m temperature are same (i.e., 10 min). (b) Same as Figure 6a but for type Ib observed on 1 July 2011.

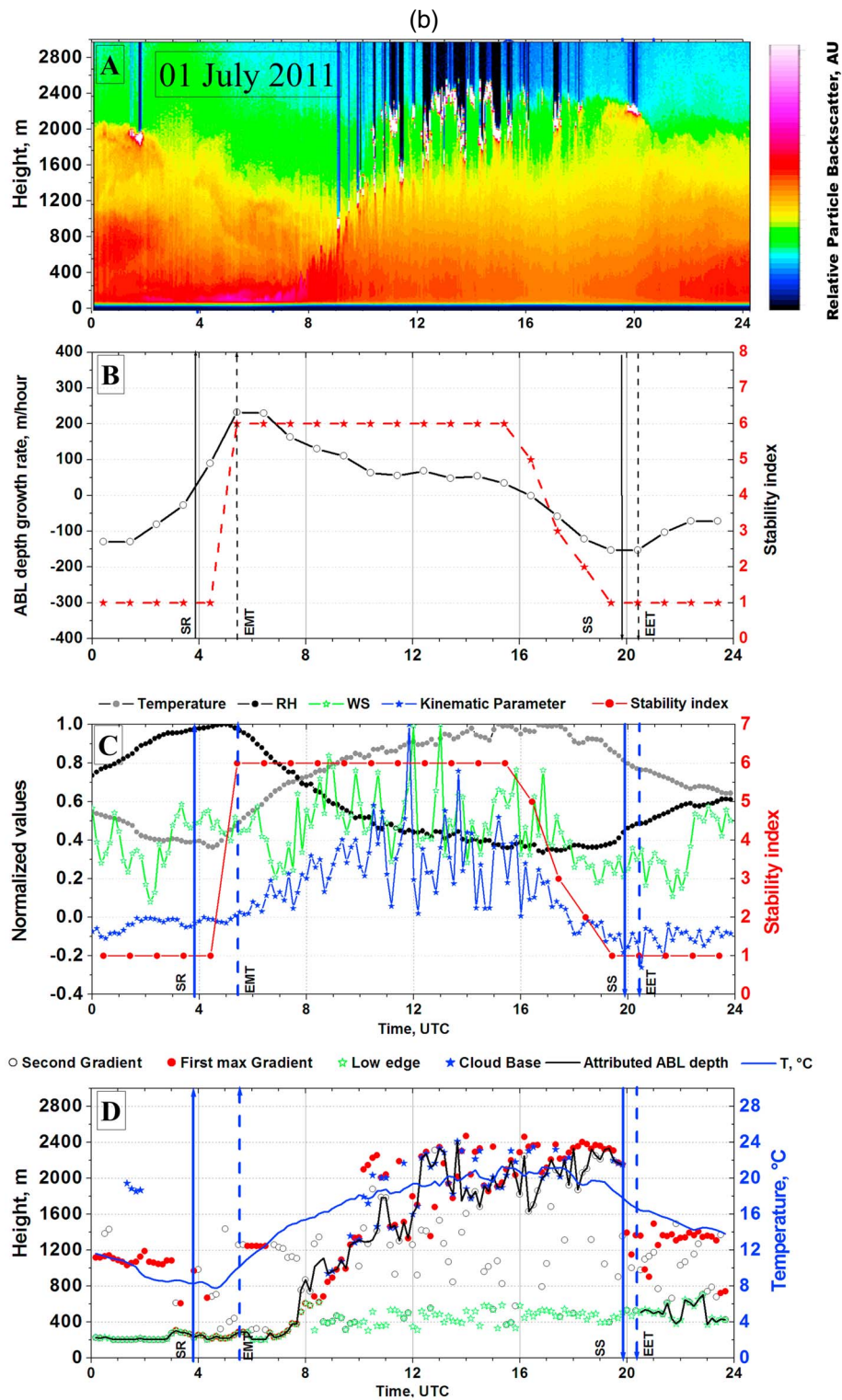


Figure 6. (continued)

clear-sky conditions, see Table 2). The upper three panels in the figure display the analyzed data for the retrieval of ABL depths while the bottom panel presents the finally attributed instantaneous ABL depths. The time-height cross section of the range-squared corrected aerosol backscatter signal

intensity obtained on 26 June 2011 is presented in the top panel. This is an example of the lidar measurements between ground and 2000 m AGL during a typical clear-sky day at SIRTa. The second panel from top shows the time series of the stability index and ABL depth growth rates

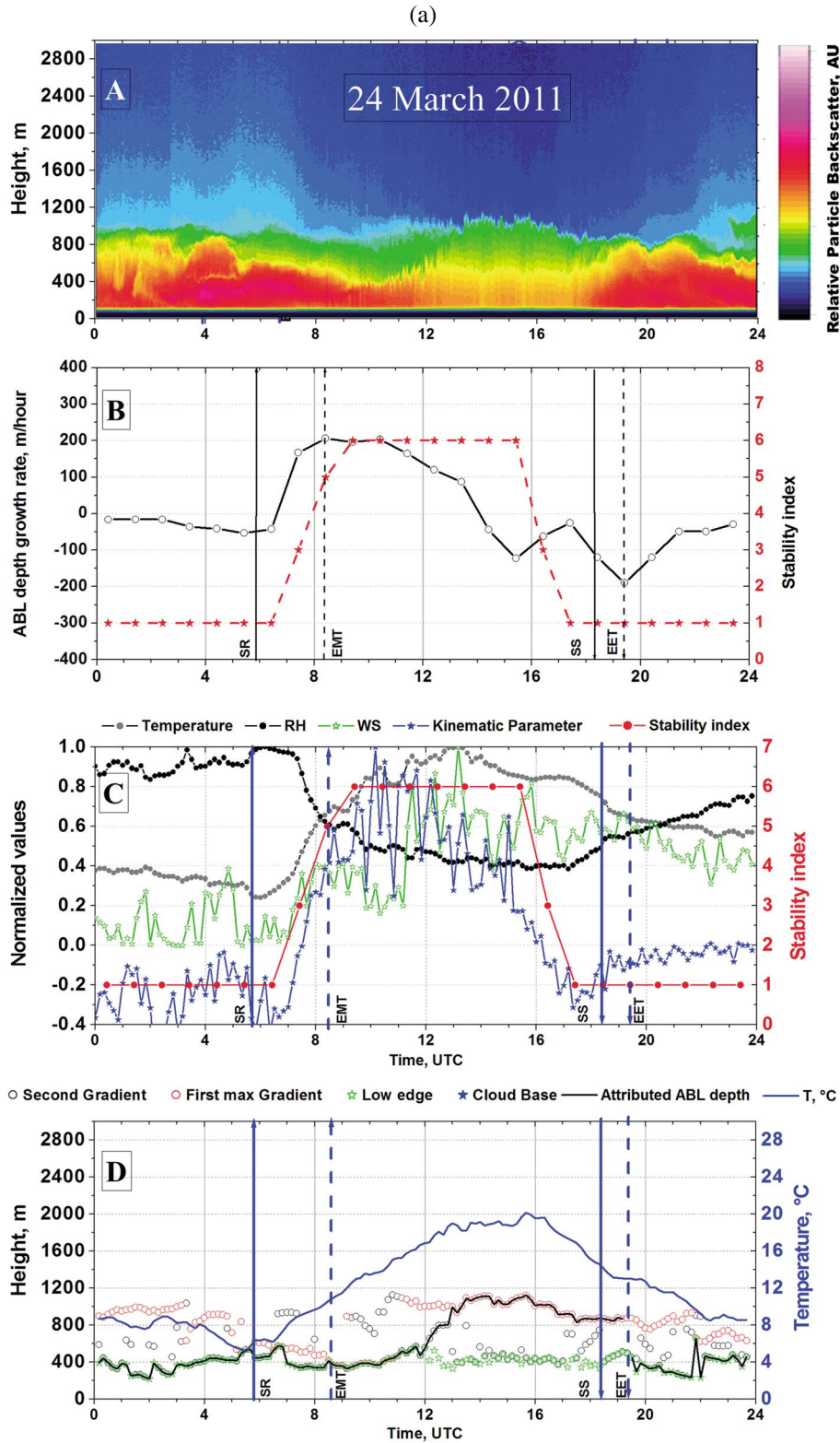


Figure 7. Same as Figure 6 but for type IIa (24 March 2011) and IIb (9 March 2011).

that help determine the end of the EMT and the EET periods (see vertical dotted lines). The growth rates shown are not obtained using the lidar measurements but the encroachment model. Times of sunrise (SR) and sunset (SS) for

SIRTA are also marked in all panels in Figure 6a (see vertical solid lines). The third panel from top presents the time series of kinematic parameter, near-surface temperature, relative humidity, and wind speed after they are normalized with their

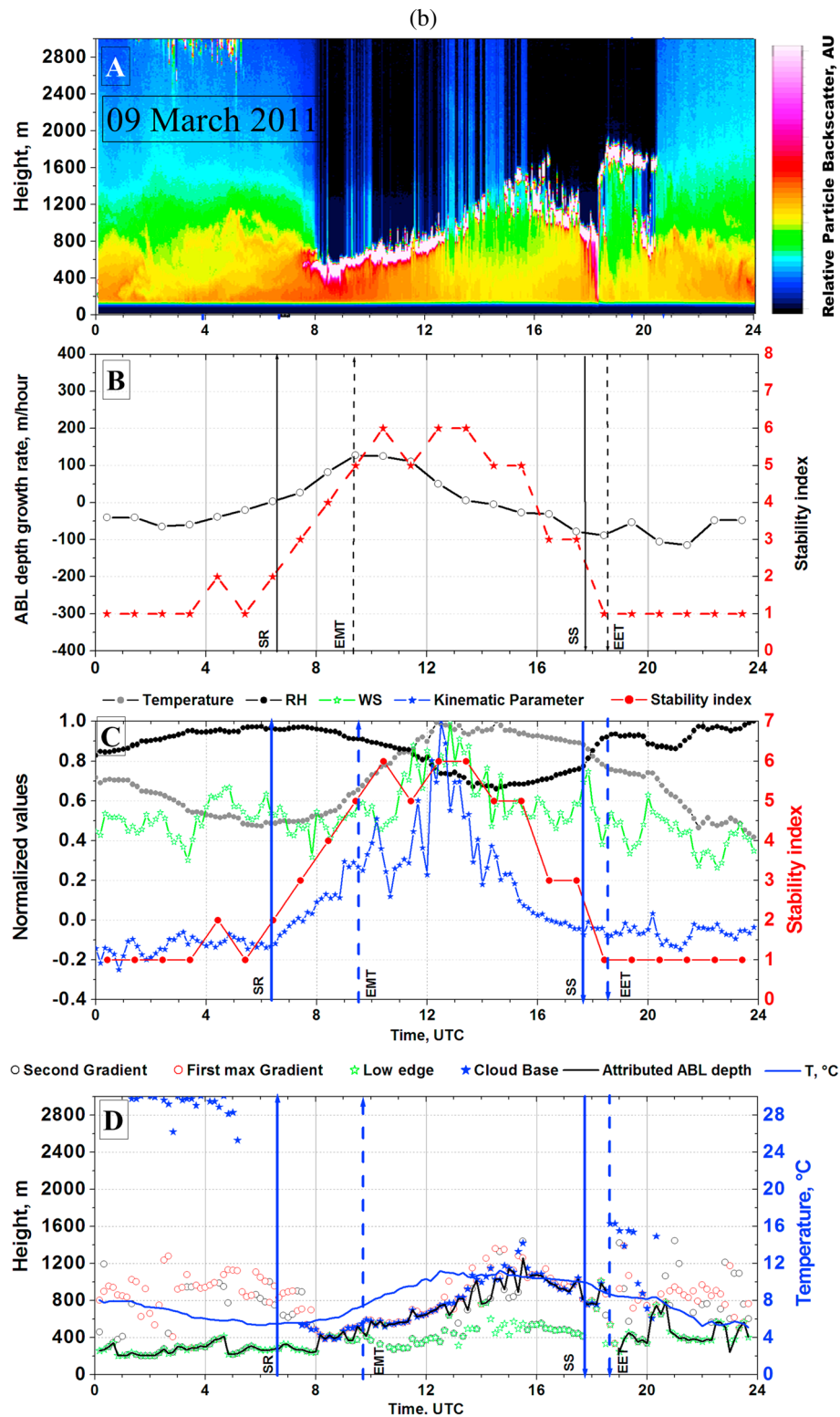


Figure 7. (continued)

maximum values. Such normalization helps detect the shape of the diurnal cycle (thus, temporal evolution) of these parameters to robustly determine the times of two transitions. The bottom panel displays the locations of three key aerosol gradients and

cloud base heights and the attributed ABL top height. The diurnal cycle of 2 m temperature is also overlaid.

[32] A sharp decrease in the relative humidity can be well observed from the figure (the second panel from top in

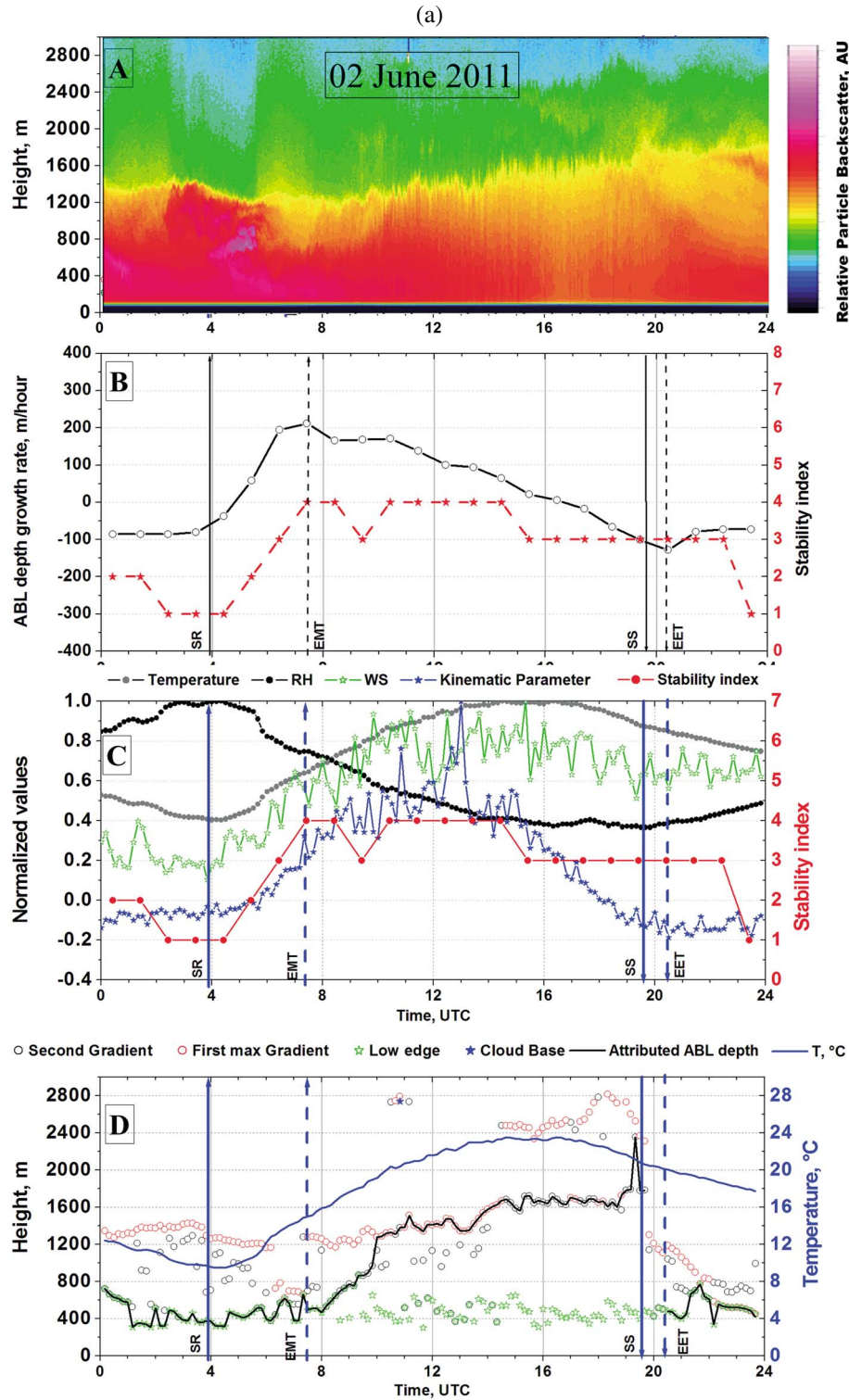


Figure 8. Same as Figure 6 but for type IIIa (2 June 2011) and IIIb (13 July 2011).

Figure 6a) while a slow increase in temperature during the EMT period after sunrise is observed. The onset of the CBL development triggers a dilution of water vapor; thus, a sharp decrease in the mixing ratio is observed. On the other hand, during the EET period, once the boundary layer turbulence is reduced, mixing of passive tracers like water vapor decreases;

hence, their higher concentration are observed; however, an increase in the mixing ratio can be well detected before the sunset when the turbulence intensity already has started decreasing. *Acevedo and Fitzjarrald* [2001] attributed advection to be an important factor in governing the time and nature of the rise in the mixing ratio while *Busse and Knupp* [2012]

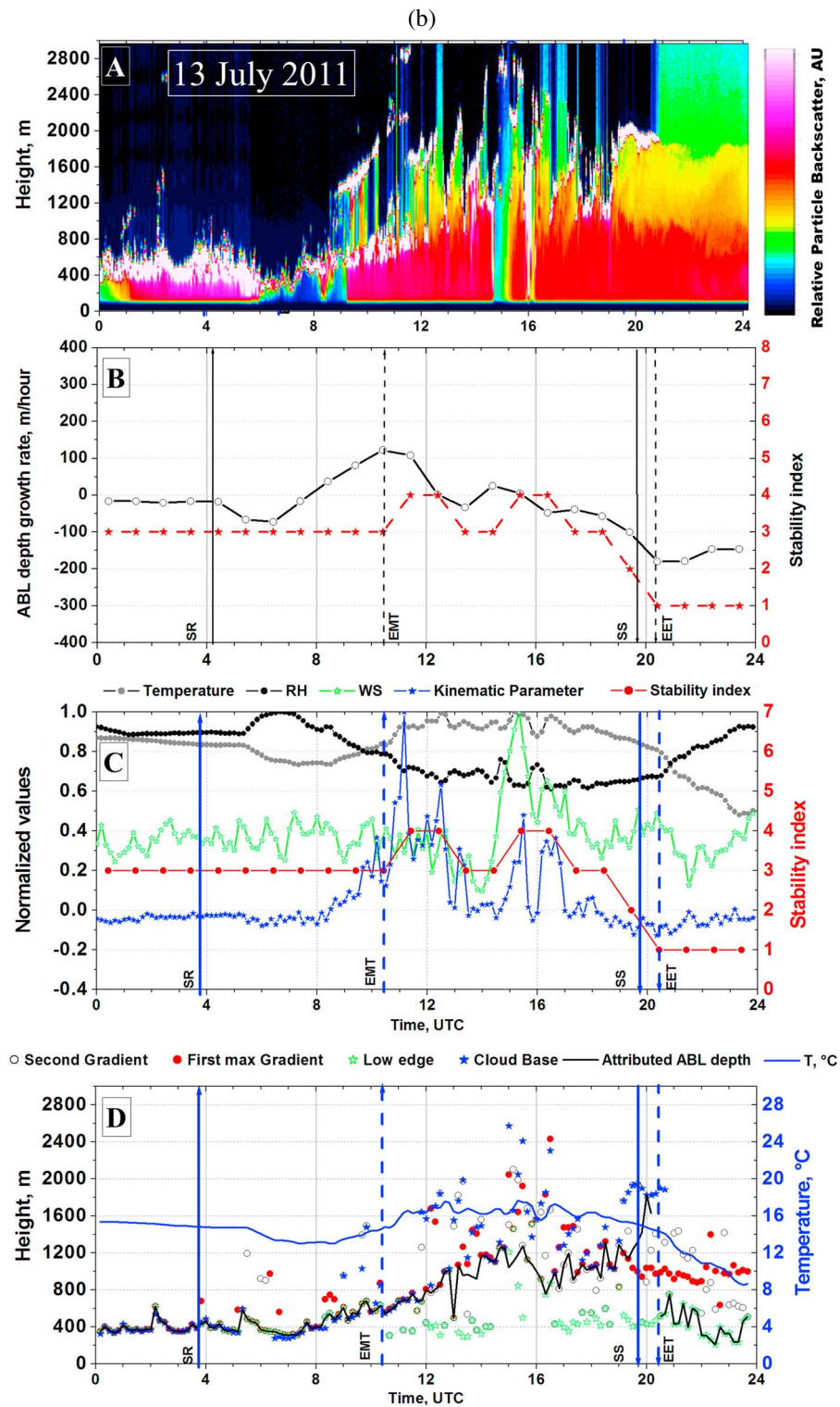


Figure 8. (continued)

found a range of periods for the sharp increase in the mixing ratio as a result of prevailing synoptic conditions. Therefore, we did not use the variability of mixing ratio to detect the transition periods.

[33] For the case presented in Figure 6a, crossover during the EMT takes place at 05:30 UTC after sunrise at 03:58

UTC and the end of the EMT at 06:40 UTC while the end of EET takes place at 20:40 UTC following sunset at 19:50 UTC. A clear diurnal cycle of the stability index can be observed: stable conditions at night and unstable or very unstable conditions during the well-mixed CBL in the daytime. Figure 6b plots a typical example case for type Ib

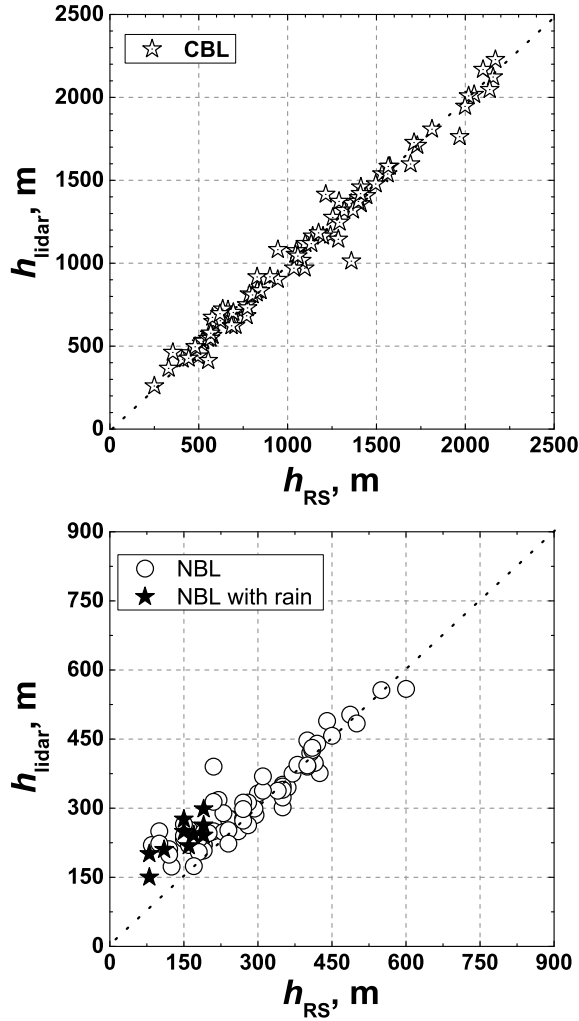


Figure 9. Scatterplots showing comparisons of the ABL depth estimates obtained by the newly developed attribution technique and the nearby radiosonde measurements for both the daytime CBL (upper panel) and the NBL (lower panel) regimes. Radiosonde retrievals are used as the common reference for both regimes. A 1:1 line (dashed gray) is overlaid on each panel for comparison. Correlation coefficients obtained are 0.968 and 0.928 for the daytime (87 cases) and nighttime (81 cases) measurements, respectively. In the lower panel, solid stars mark the cases with precipitation at the lidar site.

when Cu-topped CBL regime prevailed between 09:00 and 18:00 UTC on 01 July 2011. The stability index once again shows here a direct transition. Like type I, near-surface meteorological measurements confirm a steady increase in temperature and decrease in relative humidity during the EMT. A particular difference between two types of transitions is that the CBL depths grow much more rapidly for type Ib than for Ia. Clearly visible is the EET time and evolution of NBL depths after 20:30 UTC while the RL is still present at an altitude of around 1400 m AGL. The NBL depths are slightly more elevated than the previous day's NBL depths observed in the morning.

[34] Figures 7a and 7b plot two cases for type II for a clear day (IIa, 24 March 2011) and a cloudy day (IIb, 09 March

2011), respectively; for both cases, an indirect transition in the stability index takes place at the end of the EMT. Type IIb exemplifies that because of the optically thick clouds within the ABL, the aerosol backscatter signal intensity is highly attenuated so that all STRTA-2D derived layers exist within the altitudes below 1600 m except some cloud layers at 3000 m AGL around dawn. The ABL depth growth rates estimated for the attribution also are found to be around 100 m/h (0.028 m/s).

[35] Figures 8a and 8b display two cases for type III for a clear-sky day (type IIIa, 2 June 2011) and a day with an extensive cloud deck in the lowermost ABL present more than 20 h (type IIIb, 13 July 2011). The stability index does not show any clear transition on these days so it is not possible to identify the end of the EMT and the EET using the criteria of the stability index. Therefore, the times corresponding to the end of EMT and the EET are determined from the maximum and minimum growth rates of ABL depths, respectively, since we found earlier that stability index-based transitions and changes in the growth rates show similar results. The ABL is shallower for type IIIb than that observed for type IIIa.

6.2. Evaluation of the ABL Depth Estimates

[36] For the evaluation of the lidar-derived finally attributed instantaneous ABL depths (henceforth lidar-derived ABL depths only), we compare the results to the radiosonde measurements of ABL depths at 00:00 and 12:00 UTC. For the daytime measurements of ABL depths from RS data sets, we use the most widely accepted method based on the profiles of bulk Richardson number (R_{ib}) which is calculated as

$$R_{ib}(z) = \frac{g(z - z_0)}{\Theta_v(z_0)} \frac{\Theta_v(z) - \Theta_v(z_0)}{u(z)^2 + v(z)^2}$$

where g is the gravitational acceleration, Θ_v is the virtual potential temperature, z_0 is the lowest measurement level (about 20 m AGL), and u and v are the zonal and meridian wind components [Stull, 1988; Seibert *et al.*, 2000]. The top of the ABL is defined by the height at which R_{ib} is greater than the critical bulk Richardson number (R_{ibc}) of 0.21 [e.g., Menut *et al.*, 1999]. Since the Richardson number method is suitable only for well-mixed CBL regimes [Seibert *et al.*, 2000], we use the vertical profiles of the mean horizontal wind speed and potential temperature to determine the NBL depths following the method described in Liu and Liang [2010]. In this method, the regime identification is first performed by examining the near-surface thermal gradient between the fifth and second levels and then compared with a predefined potential temperature increment for the minimum strength of the stable (inversion) layer below the NBL top (see Liu and Liang [2010] for further details). Because of the intermittent and weak turbulence structure of the NBL, features of NBL are entirely different from the unstable CBL [Seibert *et al.*, 2000]; thus, the definition of the depth although clear for the CBL is less clear for the NBL as its top may blend into the RL above. In particular, the SBL turbulence can result from two dominant mechanisms: buoyancy forced and/or shear driven. Following Liu and Liang [2010], we defined the NBL top to be the level of the LLJ nose if present. However, in the situations,

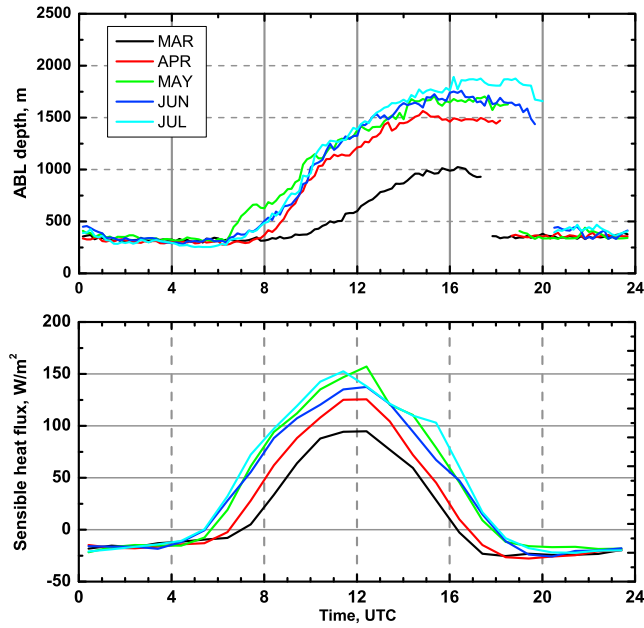


Figure 10. Monthly mean diurnal cycles of ABL depths (upper panel) and surface-level sensible heat flux (lower panel) for different months where composite diurnal cycles of ABL depths and heat fluxes for all measurements obtained during each month were considered. Harmonized colored lines are used in both panels.

when the “nose” of the nocturnal LLJ is not found, we use only the profiles of the potential temperature gradient [e.g., Joffre *et al.*, 2001].

[37] The intercomparison results both for the daytime CBL and the NBL for a total of 168 cases are presented in Figure 9 which clearly indicate a high correlation between the lidar and RS-derived results. In particular, for the daytime CBL depths, an excellent concordance is found with a linear regression coefficient (R^2) of 0.968. The remaining uncertainties can be mainly attributed to the application of two different approaches (thermodynamic profiles for RS and aerosol gradients for lidar), sampling of different air masses for the spatial separation of ~ 12 km between two sites, drifts of the RS due to prevailing wind, and advection of aerosol particles, as was found previously by many researchers [e.g., Haeffelin *et al.*, 2012].

[38] For the NBL cases, we found a correlation coefficient of 0.927 with comparatively larger number of scatter than obtained for daytime observations. In particular, the lidar-based approach resulted in a systematic overestimation for the lower NBL depths that ranges from 50 to 200 m AGL. This occurs because the full overlap between the laser beam and the field of view of the receiving telescope of the lidar (the so-called overlap factor of lidar transceiver) is reached at an altitude of around 150 m AGL below which the measured aerosol backscatter signals are not useful. Thus, during the situations when the NBL depths are shallower than 150 m, lidar-derived NBL depths are likely overestimated. However, the aforementioned factors for the inconsistencies in the daytime measurements cannot be completely ruled out for the NBL regime.

[39] Additionally, we notice that some of the higher discrepancies are found during the evenings when there was precipitation for more than an hour at the lidar site before the time of the RS launches. Ten such cases are identified which illustrated that the lidar measurements overestimated the NBL depths by at least 100 m compared to the RS that showed shallow NBL depths between 80 and 170 m AGL. These cases are marked by black stars in the lower panel of Figure 9. We analyzed the 24 h cumulated precipitation measurements at SIRTa to identify the days with precipitation. In general, atmospheric processes like precipitation result in a noticeable removal of aerosols because of the wet scavenging of the aerosol particles by raindrops [e.g., Berthet *et al.*, 2010]; in such situations, aerosol gradients are not determined well by lidar. Thus, the attribution technique could have resulted in erroneous values of NBL depths during or immediately following precipitation.

[40] An overall statistics of the intercomparison results delineated that for the CBL regimes, lidar and RS determination are consistent within 150 m for 94% cases. Similar analyses for the NBL depths revealed consistency within 50 m for

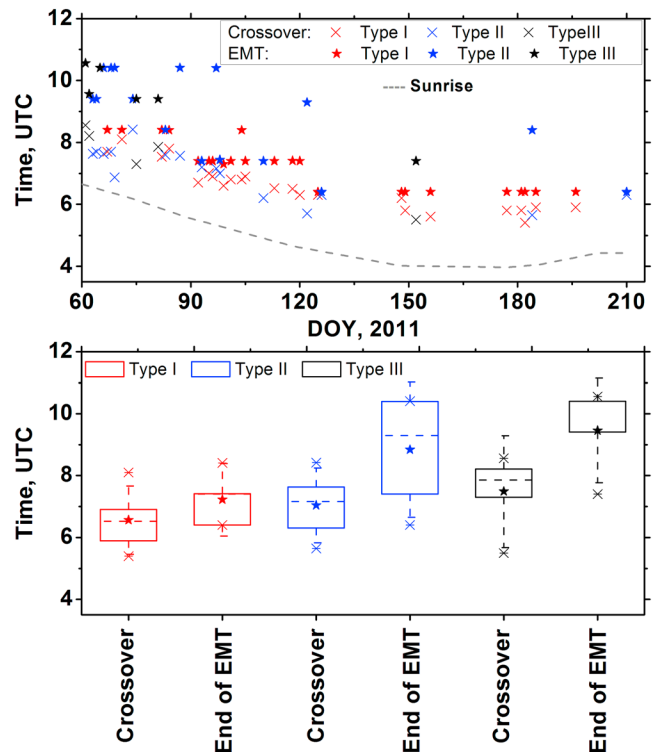


Figure 11. Upper panel: Times of sunrise, crossover, and the end of EMT (in UTC) on different days of the year (DOY) 2011. A trend like the temporal changes in the sunrise time from March to July can be observed for the crossover; however, they are not identical. Lower panel: a box and whisker plot of the times for the crossover and EET for the three different types of transitions. In each box, the dashed line indicates the median and the extent of boxes, 25th and 75th percentiles; whiskers represent the standard deviation. The central point is the mean value and the external points are the maximum and minimum.

67% cases. These results clearly indicate a substantial improvement in the STRAT-2D analyses reported by *Haefelin et al.* [2012] where they found these consistencies to be 67% and 33% for the daytime and nighttime measurements (within a limit of 300 m), respectively. Thus, the results reported here clearly emphasize the impact of the geophysical process-based attribution technique on the STRAT-2D results.

6.3. Diurnal Cycle of the ABL Depth

[41] The high-resolution (10 min) time series of the ABL depths obtained between March and July 2011 are analyzed to determine the mean monthly diurnal cycle of ABL depths (Figure 10). To achieve this, we exclude the days with extensive cloud cover and precipitation. The CBL depths and NBL depths determined for different days in a month are averaged separately so that the onset of NBL after EET can be clearly distinguished; this resulted in discontinuities in the composite diurnal cycle of each month.

[42] The maximum ABL depths are mostly observed in the early afternoon. An increasing trend in the daytime maximum ABL depths from 1025 m AGL in March to 1892 m AGL in July can be also observed. A significant increase in the daytime maximum ABL depths from March to April can be seen from the figure while from April to July a more gradual increase is observed. The lower panel in Figure 10 displays the monthly mean diurnal cycle of surface-level sensible heat flux for different months. Unlike monthly mean diurnal cycle of ABL depths, a gradual decrease in the sensible heat flux can be seen. However, a considerable increase in the heat flux is observed from March to April that likely triggered a significant increase in the ABL depths from March to April. In general, these results are similar to that reported by *Haefelin et al.* [2012] and thus climatologically consistent.

[43] The ABL depths during the afternoon are quasi-stationary without any significant growths for more than 3 h for all five months. The interval during which the CBL is quasi-stationary increased monotonically from March (3.2 h) to July (6.3 h) as expected because of the increase in the length of the days from spring to summer. A shift from the late morning to the early morning in the onset and growth of the CBL from March to July can also be observed. On the other hand, it is found that the onset of NBL during the EET can occur at significantly different times in each month. A progression of the time of transition from CBL to NBL to later in the day from March to July is observed.

6.4. Characteristics of the Crossover and the EMT

[44] To investigate the observed characteristics of the crossover and the EMT, in particular, their timings, we mainly consider clear days without extensive cloud cover or precipitation; however, days with Cu clouds at the developing CBL top are not excluded from this analysis. The upper panel in Figure 11 shows the daily variation of the times of sunrise, crossover, and the end of EMT on different days; three types of transitions are marked with different symbols. We find that type I, type II, and type III are observed for 35%, 40%, and 25% of all measurement days, respectively. A general temporal tendency of

type I for both crossover and EMT can be seen illustrating earlier transition times in the summer than in the spring while type II and III did not indicate such a clear tendency. Instead, a rather large number of scatters both for crossover and the end of EMT timings are found. A box-and-whisker plot of the corresponding measurements is also shown which illustrates that the type II crossover and EMT contains the largest scatter. The end of EMT, hence the onset of ABL growth, is delayed for type II and type III compared to type I while the crossover time averaged over all cases does not evince such significant delays in those types. For type II, the transition of atmospheric stability from stable to unstable/very unstable regime does not take place directly but through neutral/near neutral phase. A slower increase in the CBL is, in general, found so that a shallow CBL is first developed before the rapid rise. Once the nocturnal inversion is completely eroded, a faster growth can be observed. However, type II cases are predominantly observed during March and April when the sun rises at a later time compared to the months in summer so that a seasonal bias cannot be completely ruled out. Further long-term measurements will help illustrate the seasonal dependencies of the crossover and EMT for the three different types of transitions.

[45] Figure 12 plots the time series of the temporal delay between sunrise and crossover (the top left hand panel) and the delay between the end of EMT and crossover (the bottom left hand panel). These results help illustrate the time required for the crossover to take place relative to the time of sunrise and the end of EMT relative to the crossover. Different colored symbols mark three types of transitions. The corresponding box-and-whisker plots are also shown (the top right and bottom right panels). Temporal delays between crossover and sunrise are not significantly different (around 1.5 h) for three types of transitions; less variability can be observed for type I than for the other two types. However, the temporal delay between crossover and end of EMT is not independent on the types of transitions. The corresponding box-and-whisker plot also shows that the mean value of the delay between the crossover and the end of EMT is lower for type I (40 min) than for type II and type III (1 h and 50 min).

[46] Two phases during the EMT period (sunrise to crossover and crossover to the end of EMT) decipher different but interesting characteristics. For instance, earlier crossover does not necessarily trigger an early onset of CBL development. On average, type I transition takes around 2.4 h from sunrise to the end of EMT while type II and III take more than 3.2 h. Thus, the time required to erode the nocturnal inversion depends on the stability regimes and hence on the types of transitions during the EMT period. The results presented here for the delay between sunrise and crossover is similar to the results reported previously by *Angevine et al.* [2001] while the characteristics of the shallow CBL are similar to that reported by *Bange et al.* [2007]. However, the delay between the onset of CBL development and the crossover are not similar because the maximum height of measurements in *Angevine et al.* [2001] was constrained by the height of a tower and the resolution with which vertical profiles were obtained. Additionally, the definition of the EMT in our study is based on the changes in stability indices.

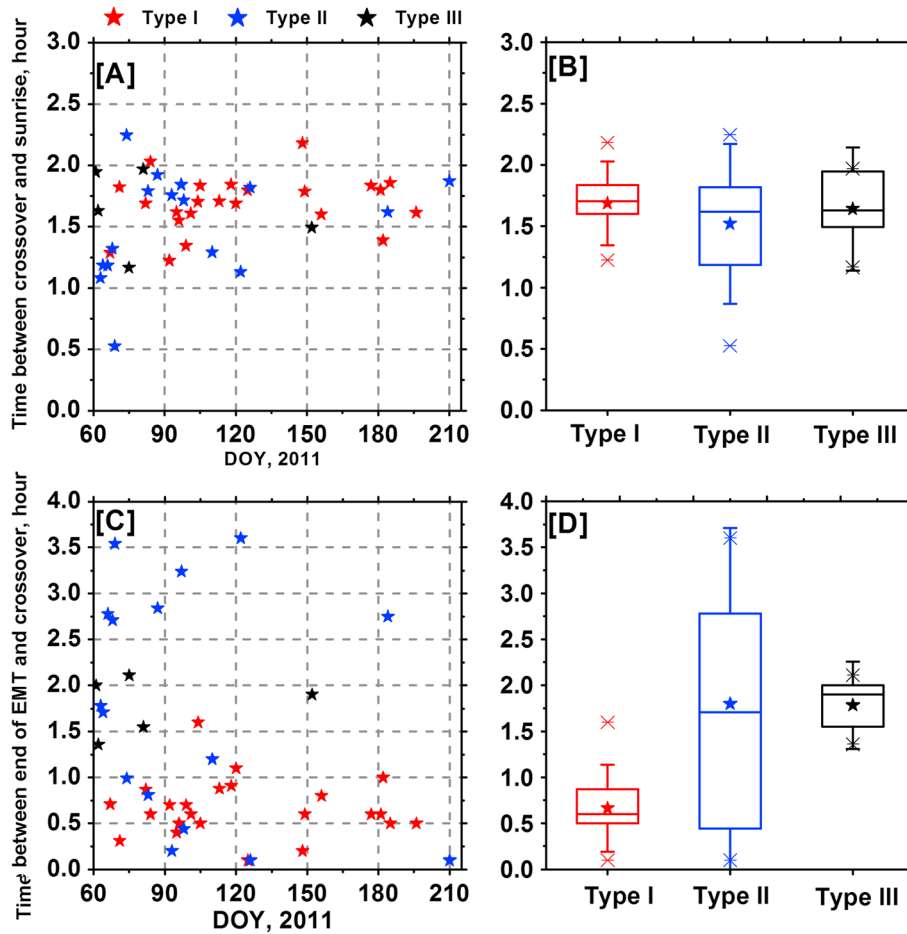


Figure 12. (a) Daily variability in the temporal delay from sunrise to crossover for three different transitions types observed during the EMT with (b) corresponding box and whisker plot. (c) Delay from crossover to the end of EMT with (d) corresponding box and whisker plot. Whisker and box levels are similar as in Figure 11 but for the temporal delays between crossover and sunrise (Figure 12b) and the end of EMT and crossover (Figure 12d).

7. Summary, Conclusion, and Outlook

[47] Within this paper, we described the major components of a newly developed technique for a geophysical process-based attribution to determine the ABL depths from routine lidar observations obtained between March and July 2011 over SIRTa observatory in France. The major components of the attribution technique are (1) STRAT-2D algorithm for the determination of three key gradients in the aerosol stratification and cloud base height, (2) variance-based analysis to retrieve ABL turbulence features illustrating maximum variability of particle backscatter and hence to estimate the mean ABL depth, and (3) the analyses of near-surface micrometeorological measurements to determine the EMT and the EET periods of a day to separate the daytime CBL and the NBL regimes. Stability index derived using Obukhov length, L , served as an excellent indicator for this purpose. Finally, we combine the above three components for the attribution of “true” ABL top height. Choice of the “relevant” minimum in the gradient corresponding to the ABL top is facilitated by combining the variance and the gradient method retaining its greater robustness against extraneous backscatter peaks usually obtained by applying only the

gradient technique on the high-resolution lidar profiles. To the best of our knowledge, for the first time, the effect of near-surface meteorological conditions, in particular, the observed EMT and EET on the boundary layer stratification and variability of the ABL depths during entire diurnal cycle, is investigated in detail.

[48] Using the five months measurements, we could investigate different thermal, stability, and dynamical regimes of ABL depths and their variability during diverse meteorological situations. An excellent agreement was found between lidar-derived and radiosonde-based estimations of ABL depths with a correlation coefficient of 0.968 and 0.927 for daytime and nighttime measurements, respectively. The first results obtained with the new attribution technique are promising so that the routine analysis of the lidar data sets can be performed for determining the ABL depths over different ICOS supersites in Europe [Ramonet *et al.*, 2011] or for any other lidar network.

[49] By defining three different types of transitions based on the stability index, we classified the ABL circulations patterns in three major types, namely types I, II, and III; on the basis of the measurements performed for more than 100 days, different characteristic features of these types

were studied. For instance, when near-surface meteorological regime changes rapidly from stable to unstable/very unstable regime (type I, a direct transition in the stability index), an almost instantaneous mixing of the new boundary layer with the air masses in the RL and FA takes place confirming the fact that the buoyant thermals that originate at the surface reach the RL without passing through a stable atmospheric layer (often called “overshooting”). The mean daytime ABL depths showed large month-to-month variability (e.g., mean March and July peaks are ~ 1000 and 1800 m, respectively) while the monthly mean NBL depths evinced much smaller differences among different months of two seasons. These results are climatologically consistent for the region around Paris.

[50] Further long-term measurements will help better understand the interaction among the synoptic regimes, boundary layer turbulence features, and ABL depths and hence the roles of key forcing mechanisms in governing diurnal variability of ABL depths in particular during the early morning and the early evening transition periods. Additionally, we plan to apply the new attribution technique on ceilometer measurements within near future research activities, in particular, to facilitate the monitoring of shallow NBL depths since present-day ceilometers (e.g., CL31) have, in general, very low optical overlap height (~ 45 m).

[51] **Acknowledgments.** This research was partly funded by the project ICOS-France (<http://icos-infrastructure-france.lsce.ipsl.fr/>). The authors would like to extend their acknowledgments to the staff of the SIRTa atmospheric observatory for providing the micrometeorological data sets and the lidar measurements. Thanks are also due to Météo-France for the Trappes radiosonde profiles. Fruitful discussion with M. Ramonet and M. Schmidt (LSCE, France) is highly acknowledged. The research project is also related to COST ACTION ES0702 EG-CLIMET (<http://www.eg-climet.org/>). We also would like to thank three anonymous reviewers for their objective assessments and very useful suggestions which helped improve the scientific and technical contents of the article. We thank very much Temple R. Lee (Department of Environmental Sciences, University of Virginia, VA, USA) for his careful proofreading.

References

- Acevedo, O. C., and D. Fitzjarrald (2001), The early evening surface-layer transition: temporal and spatial variability, *J. Atmos. Sci.*, **58**, 2650–2667.
- Angevine, W. M., H. K. Baltink, and F. C. Bosveld (2001), Observations of the morning transitions of the convective boundary layer, *Boundary Layer Meteorol.*, **101**, 209–227.
- Bange, J., T. Spiess, and A. V. Kroonenberg (2007), Characteristics of the early-morning shallow convective boundary layer from Helipod flights during STINHO-2, *Theor. Appl. Climatol.*, **90**, 113–126.
- Batchvarova, E., and S.-E. Gryning (1991), Applied model for the growth of the daytime mixed layer, *Boundary Layer Meteorol.*, **56**, 261–274.
- Batchvarova, E., and S.-E. Gryning (1994), An applied model for the height of the daytime mixed layer and the entrainment zone, *Boundary Layer Meteorol.*, **71**, 311–323.
- Behrendt, A., et al. (2011a), Observation of convection initiation processes with a suite of state-of-the-art research instruments during COPS IOP 8b, *Q. J. R. Meteorol. Soc.*, **137**(S1), 81–100.
- Behrendt, A., S. Pal, V. Wulfmeyer, A. M. Valdebenito, and G. Lammel (2011b), A novel approach for the characterization of transport and optical properties of aerosol particles near sources. Part I: Measurement of particle backscatter coefficient maps with a scanning UV lidar, *Atmos. Environ.*, **45**, 2,795–2,802.
- Berthet, S., M. Leriche, J.-P. Pinty, J. Cuesta, and G. Pigeon (2010), Scavenging of aerosol particles by rain in a cloud resolving model, *Atmos. Res.*, **96**, 325–336.
- Bianco, L., I. V. Djalalova, C. W. King, and J. M. Wilczak (2011), Diurnal evolution and annual variability of boundary-layer height and its correlation to other meteorological variables in California’s central valley, *Boundary Layer Meteorol.*, **140**, 491–511.
- Busse, J., and K. Knupp (2012), Observed characteristics of the afternoon-evening boundary layer transition based on sodar and surface data, *J. Appl. Meteorol. Hydrol.*, **51**, 571–582.
- Caughey, S. J., J. C. Wyngaard, and J. C. Kaimal (1979), Turbulence in the evolving stable boundary layer, *J. Atmos. Sci.*, **36**, 1041–1052.
- Couvreur, F., F. Guichard, V. Masson, and J.-L. Redelsperger (2007), Negative water-vapour skewness and dry tongues in the convective boundary layer: Observations and large-eddy simulation budget analysis, *Boundary Layer Meteorol.*, **123**, 269–294.
- Di Giuseppe, F., A. Riccio, L. Caporaso, G. Bonafé, G. P. Gobbi, and F. Angelini (2012), Automatic detection of atmospheric boundary layer height using ceilometer backscatter data assisted by a boundary layer model, *Q. J. R. Meteorol. Soc.*, **138**, 649–663.
- Emeis, S., C. Jahn, C. Munkel, C. Münsterer, and K. Schäfer (2007), Multiple atmospheric layering and mixing-layer height in the Inn valley observed by remote sensing, *Meteorol. Z.*, **16**, 415–424.
- Eresmaa, N., A. Karppinen, S. M. Joffe, J. Räsänen, and H. Talvitie (2006), Mixing height determination by ceilometer, *Atmos. Chem. Phys.*, **6**, 1485–1493.
- Eresmaa, N., J. Härkönen, S. M. Joffe, D. M. Schultz, A. Karppinen, and J. Kukkonen (2012), A three-step method for estimating the mixing height using ceilometer data from the Helsinki testbed, *J. Appl. Meteorol. Climatol.*, **51**, 2172–2187.
- Gan, C.-M., Y. Wu, B. L. Madhavan, B. Gross, and F. Moshary (2011), Application of active optical sensors to probe the vertical structure of the urban boundary layer and assess anomalies in air quality model PM_{2.5} forecasts, *Atmos. Environ.*, **45**, 6613–6621.
- Granados-Muñoz, M. J., F. Navas-Guzmán, J. A. Bravo-Aranda, J. L. Guerrero-Rascado, H. Lyamani, J. Fernández-Gálvez, and L. Alados-Arboledas (2012), Automatic determination of the planetary boundary layer height using lidar: One-year analysis over southeastern Spain, *J. Geophys. Res.*, **117**, D18208, doi:10.1029/2012JD017524.
- Gryning, S., E. Batchvarova, B. Brümmner, H. Jørgensen, and S. Larsen (2007), The extension of the wind profile over homogeneous terrain beyond the surface boundary layer, *Boundary Layer Meteorol.*, **124**, 251–268.
- Haefelin, M., et al. (2005), SIRTa, a ground-based atmospheric observatory for cloud and aerosol research, *Ann. Geophys.*, **23**, 253–275.
- Haefelin, M., et al. (2012), Evaluation of mixing-height retrievals from automated profiling lidars and ceilometers in view of future integrated networks in Europe, *Boundary Layer Meteorol.*, **143**, 49–75.
- Haman, C. L., B. Lefer, and G. A. Morris (2012), Seasonal variability in the diurnal evolution of the boundary layer in a near-coastal urban environment, *J. Atmos. Oceanic Technol.*, **29**, 697–710.
- Hogan, R. J., A. L. M. Grant, A. J. Illingworth, G. N. Pearson, and E. J. O’Connor (2009), Vertical velocity variance and skewness in clear and cloud-topped boundary layers as revealed by Doppler lidar, *Q. J. R. Meteorol. Soc.*, **135**, 635–643.
- Joffe, S. M., M. Kangas, M. Heikinheimo, and S. A. Kitaigorodskii (2001), Variability of the stable and unstable atmospheric boundary layer height, *Boundary Layer Meteorol.*, **99**(3), 429–450.
- Kaimal, J. C., and J. J. Finnigan (1994), *Atmospheric Boundary Layer Flows: Their Structure and Measurement*, Oxford University Press, Cambridge, pp. 289.
- Kaimal, J. C., J. C. Wyngaard, D. A. Haugen, O. R. Coté, and Y. Izumi (1976), Turbulence structure in the convective boundary layer, *J. Atmos. Sci.*, **33**, 2152–2169.
- Lammert, A., and J. Bösenberg (2006), Determination of the convective boundary layer height with laser remote sensing, *Boundary Layer Meteorol.*, **119**, 159–170.
- Lenschow, D. H., V. Wulfmeyer, and C. Senff (2000), Measuring second through fourth-order moments in noisy data, *J. Atmos. Oceanic Technol.*, **17**, 1330–1347.
- Lenschow, D., H. M. Lothon, S. D. Mayor, P. P. Sullivan, and G. Caunt (2012), A comparison of higher-order vertical velocity statistics in the convective boundary layer from lidar with in-situ measurements and large-eddy simulations, *Boundary Layer Meteorol.*, **143**, 107–123.
- Liu, S., and X. Z. Liang (2010), Observed diurnal cycle climatology of planetary boundary layer height, *J. Clim.*, **23**, 5790–5809.
- Maronga, B., and S. Raasch (2012), Large-eddy simulations of surface heterogeneity effects on the convective boundary layer during the LITFASS-2003 experiment, *Boundary Layer Meteorol.*, doi:10.1007/s10546-012-9748-z.
- Mattis, I., A. Ansmann, D. Müller, U. Wandinger, and D. Althausen (2004), Multiyear aerosol observations with dual-wavelength Raman lidar in the framework of EARLINET, *J. Geophys. Res.*, **109**, D13203, doi:10.1029/2004JD004600.
- Menut, L., C. Flamant, J. Pelon, and P. H. Flamant (1999), Urban boundary-layer height determination from lidar measurements over the Paris area, *Appl. Opt.*, **38**, 945–954.
- Moeng, C. (1984), A large eddy simulation model for the study of planetary boundary layer turbulence, *J. Atmos. Sci.*, **41**, 2052–2062.
- Morille, Y., M. Haefelin, P. Drobinski, and J. Pelon (2007), STRAT: An automated algorithm to retrieve the vertical structure of the

- atmosphere from single-channel Lidar data, *J. Atmos. Oceanic Technol.*, 24, 761–775.
- Münkel, C. (2007), Mixing height determination with lidar ceilometers—results from Helsinki testbed, *Meteorol. Z.*, 16, 451–459.
- Nilsson, E. D., Ü. Rannik, M. Kulmala, G. Buzorius, and C. D. O'Dowd (2001), Effects of continental boundary layer evolution, convection, turbulence and entrainment on aerosol formation, *Tellus B*, 53, 441–461.
- Obukhov, A. M. (1971), Turbulence in an atmosphere with a non-uniform temperature, *Boundary Layer Meteorol.*, 2, 7–29.
- Ouwensloot, H. G., J. Vilà-Guerau de Arellano, A. C. Nölscher, M. C. Krol, L. N. Ganzeveld, C. Breitenberger, I. Mammarella, J. Williams, and J. Lelieveld (2012), Characterization of a boreal convective boundary layer and its impact on atmospheric chemistry during HUMPPA-COPEC-2010, *Atmos. Chem. Phys.*, 12, 9335–9353.
- Pal, S., and P. C. S. Devara (2012), A wavelet-based spectral analysis of long-term time series of optical properties of aerosols obtained by lidar and radiometer measurements over an urban station in Western India, *J. Atmos. Sol. Terr. Phys.*, 84, 75–87.
- Pal, S., A. Behrendt, H. Bauer, M. Radlach, A. Riede, M. Schiller, G. Wagner, and V. Wulfmeyer (2008), 3-dimensional observations of atmospheric variables during the field campaign COPS, *IOP Conf. Ser.: Earth Environ. Sci.*, 1, 012031, doi:10.1088/1755-1315/1/1/012031.
- Pal, S., A. Behrendt, and V. Wulfmeyer (2010), Elastic-backscatter-lidar-based characterization of the convective boundary layer and investigation of related statistics, *Ann. Geophys.*, 28, 825–847.
- Pal, S., et al. (2012), Spatio-temporal variability of the atmospheric boundary layer depth over the Paris agglomeration: An assessment of the impact of the urban heat island intensity, *Atmos. Environ.*, 63, 261–275.
- Ramonet, M., et al. (2011), The ICOS Atmospheric Thematic Center, 16th WMO Expert Meeting, Wellington, New-Zealand, 25–28 October 2011.
- Seibert, P., F. Beyrich, S.-E. Gryning, S. Joffe, A. Rasmussen, and P. Tercier (2000), Review and intercomparison of operational methods for the determination of the mixing height, *Atmos. Environ.*, 34(7), 1001–1027.
- Seidel, D. J., C. O. Ao, and K. Li (2010), Estimating climatological planetary boundary layer heights from radiosonde observations: Comparison of methods and uncertainty analysis, *J. Geophys. Res.*, 115, D16113, doi:10.1029/2009JD013680.
- Stull, R. (1988), *An Introduction to Boundary Layer Meteorology*, Kluwer Academic Publishers, Dordrecht, the Netherlands.
- Tennekes, H. (1973), A model for the dynamics of the inversion above a convective boundary layer, *Atmos. Sci.*, 30, 558–567.
- Wulfmeyer, V., S. Pal, D. D. Turner, and E. Wagner (2010), Can water vapor Raman lidar resolve profiles of turbulent variables in the convective boundary layer?, *Boundary Layer Meteorol.*, 136, 253–284.